Sensitized and Self-sensitized Photocatalytic CO_2 Reduction to HCO_2^- and CO under Visible Light with Ni(II) CNC-Pincer Catalysts

Sonya Y. Manafe,[a,‡] Nghia Le,[b,‡] Ethan C. Lambert,[c,d,‡] Christine Curiac,[c,‡] Dinesh Nugegoda,[c] Sanjit Das,[a] Leigh Anna Hunt,[c] Fengrui Qu,[a] Logan M. Whitt,[a] Igor Fedin,[a] Nathan I. Hammer,[c,*] Charles Edwin Webster,[b*] Jared H. Delcamp,[c,e*] and Elizabeth T. Papish[a*]

[‡]Equal contributions

[a]Department of Chemistry and Biochemistry, University of Alabama, Shelby Hall, Tuscaloosa, Alabama 35487, United States
[b]Department of Chemistry, Mississippi State University, Hand Lab, Mississippi State, Mississippi 39762, United States
[c]Department of Chemistry and Biochemistry, University of Mississippi, Coulter Hall, University, Mississippi 38677, United States
[d]Current Address: Department of Chemistry and Biochemistry, Florida State University, Tallahassee, Florida 32306, United States
[e]Current Address: Air Force Research Labs, Materials and Manufacturing Directorate, 2230 Tenth Street, WPAFB, OH 45433-7817, United States

* Corresponding Authors

Email addresses:
nhammer@olemiss.edu
ewebster@chemistry.msstate.edu
delcamp@olemiss.edu
etpapish@ua.edu

ABSTRACT

Robust earth-abundant transition metal-based photocatalysts are needed for photocatalytic CO_2 reduction. A series of six Ni(II) complexes have been synthesized with a tridentate CNC pincer ligand composed of two imidazole or benzimidazole derived N-heterocyclic carbene (NHC) rings and a pyridyl ring with different R substituents (R = OMe, Me, H) *para* to N of the pyridine ring. These complexes have been characterized using spectroscopic, analytic, and crystallographic methods. The electrochemical properties of all complexes were studied by cyclic voltammetry under N_2 and CO_2 atmospheres. Photocatalytic reduction of CO_2 to CO and HCO_2^- was analyzed using all the complexes in the presence and absence of an external photosensitizer (PS). All of these complexes are active as photocatalysts for CO_2 reduction with and without the presence of an external PS with appreciable turnover numbers (TON) for formate (HCO_2^-) production and typically lower amounts of CO. Notably, all Ni(II) CNC-pincer complexes in this series are also active as self-sensitized photocatalysts. Complex $\mathbf{4^{Me}}$ with a benzimidazole derived CNC pincer ligand was found to be the most active self-sensitized photocatalyst. Ultrafast transient absorption spectroscopy (TAS) experiments and computational studies were performed to understand the mechanism of these catalysts. Whereas sensitized catalysis involves halide loss to produce more active complexes, self-sensitized catalysis requires some halide to remain coordinated to allow for a favorable electron transfer between the excited nickel complex and the sacrificial electron donor. This then allows the nickel complex to undergo CO_2 reduction catalysis via Ni^I or Ni^0 catalytic cycles. The two active species (Ni^I and Ni^0) demonstrate distinct reactivity and selectivity which influences the formation of CO vs. formate as the product.

TOC Graphic

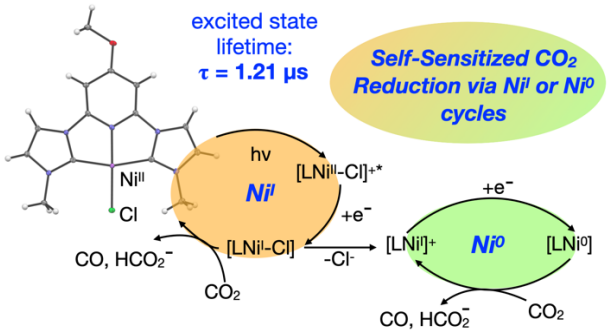

Keywords: Photocatalysis, nickel, pincer ligands, carbon dioxide reduction, self-sensitized, N-heterocyclic carbenes, organometallic compounds, ultra-fast transient absorption spectroscopy

INTRODUCTION

Increasing CO_2 emissions in the atmosphere due to fossil fuel combustion contributes to global warming and the acidification of seawater.[1-3] Light-driven CO_2 reduction to form useful chemicals (e.g. CO, formate) is a promising approach to reduce emissions,[4, 5] and formate can be used to generate electricity in fuel cells.[6, 7] However, a robust and inexpensive catalyst is needed to convert CO_2 to reduced products. Ideally, this process would be driven by sunlight photocatalytically. The use of earth-abundant metals such as Mn, Fe, Co, and Ni have been studied in the photocatalytic CO_2 reduction reaction.[4, 8-12] In 1984, Sauvage *et al.* developed a stable nickel complex with N_4-macrocycles (cyclam) with high selectivity for CO_2 reduction with faradaic efficiency up to 96% under aqueous conditions.[13] Following that, more studies of highly active and selective nickel catalysts bearing N-heterocyclic carbene (NHC) ligands for photochemical CO_2 reduction have been reported.[8, 14]

In 2018, we combined two N-heterocyclic carbenes with a pyridinol derived ring to make tridentate CNC ligands for nickel catalysts (e.g. **1**, **Figure 1**).[15] We aimed to evaluate the electronic effects on nickel CNC-pincer catalysts by using different groups (O^-, OH, H) *para* to N on the central pyridine ring.[16] Thus, we synthesized Ni complex **1** (**Figure 1**) and compared its activity as a photocatalyst for CO_2 reduction with Ni complex **2** made by Sun's group.[17] Catalyst **2** was reported to be an electrocatalyst for CO_2 reduction, but not a photocatalyst. In the presence of the photosensitizer (PS) *fac*-$Ir(ppy)_3$ and a sacrificial donor system (1,3-dimethyl-2-phenyl-2,3-dihydro-1*H*-benzo[*d*]imidazole (BIH) and triethylamine), complex **1** substituted with an O^- donor group *para* to N of the pyridine produced higher TON (10.6 TON) for CO than that of unsubstituted complex **2** (0.1 TON). This combined with the fact that the O^- group (**1**) led to greater activity *versus* the OH group in protonated **1** suggested that the oxy anion acts as a π electron

donor and plays an important role in increasing the reactivity of Ni-CNC pincer catalysts. In this study, we report a new method for the synthesis of nickel (II) CNC-pincer complexes under mild reaction conditions with moderate to high yields. Different remote substituents *para* to N on the pyridine ring of the CNC pincer are used as well as extended π conjugated systems with a benzimidazole derived NHC rings (**Figure 1**). The nomenclature used herein for this new series of nickel complexes is shown in **Table 1**.

Recently, there has been a surge in the development of sustainable earth-abundant first-row transition metal-based photocatalysts.[18] However, unlike precious metal complexes using Ru or Ir, most first-row transition metal complexes have short charge-transfer lifetimes due to low-lying ligand-field excited states.[19, 20] Doyle and co-workers proposed that Ni(II) aryl halide complexes do not require exogenous photosensitizers for light-driven cross-coupling reactions.[21] The MLCT absorption band of Ni(II) aryl halide complexes observed in the visible region experimentally decays rapidly into a long-lived ^{3}d-d state upon excitation. The weakened bonds of the ^{3}d-d state provide a pathway for photoinduced Ni–aryl bond homolysis to generate aryl radical and Ni(I) species that may be responsible for catalysis.[21, 22] Herein, we report that all six Ni(II) CNC-pincer complexes are active as photocatalysts for the formation of both formate and CO without the presence of a photosensitizer.

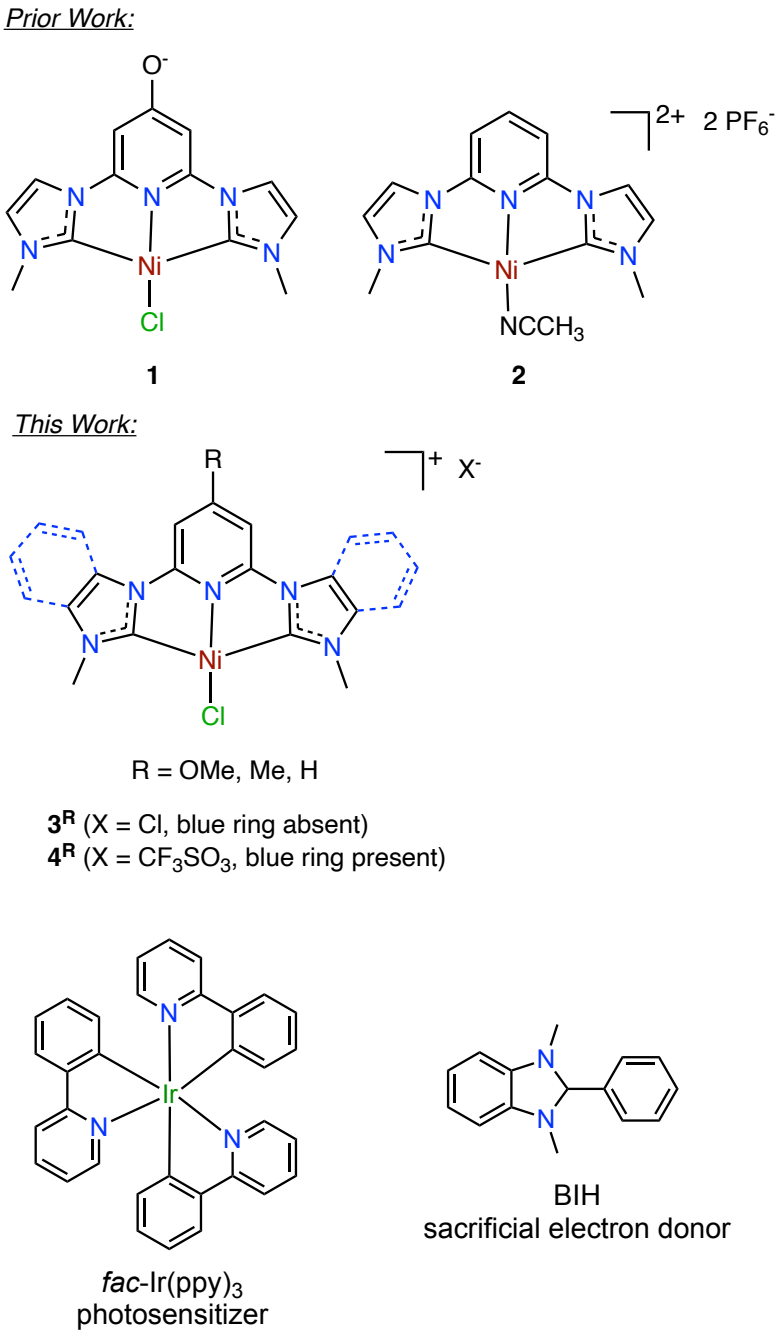

Figure 1: Nickel(II) catalysts used for sensitized and self-sensitized CO_2 reduction catalysis. Also shown are the photosensitizer and the sacrificial electron donor.

Table 1: Nickel (II) complexes designated labeling scheme.

Compound Designation	R on CNC py	Anion (X^-)
$\mathbf{3^{OMe}}$	OMe	Cl^-
$\mathbf{3^{Me}}$	Me	Cl^-
$\mathbf{3^{H}}$	H	Cl^-
$\mathbf{4^{OMe}}$	OMe	$CF_3SO_3^-$
$\mathbf{4^{Me}}$	Me	$CF_3SO_3^-$
$\mathbf{4^{H}}$	H	$CF_3SO_3^-$

Results and Discussion

Synthesis. The synthetic procedure for formation of **1** was previously reported.[15] This literature procedure required heating the CNC ligand precursor, Ni(dme)Cl_2 (dme = dimethoxyethane), and Na_2CO_3 at 50 ºC and then 160 ºC in dimethyl sulfoxide, which resulted in demethylation of the methoxy group on the pincer pyridyl ring to form complex **1** (**Scheme 1**). Milder reaction conditions were needed to avoid demethylation.[2, 8, 23-25] By using acetonitrile as the solvent, triethylamine (TEA) as the base, and a lower temperature of 60 ºC, several CNC pincer nickel complexes were synthesized without modification of the pincer R groups (**Scheme 1**). This procedure is similar to our published methods for the synthesis of Ru CNC pincer complexes.[25, 26] These nickel complexes were precipitated out of the reaction mixture as yellow to orange solids in moderate to high yield, and they have limited solubility in common organic solvents. Despite similar conditions, the imidazole and benzimidazole-derived products contain different counter anions as shown in the ^{19}F-NMR spectra and the crystal structures (**Scheme 1** and **Table 1**). All the nickel complexes were characterized by spectroscopic and analytic techniques.

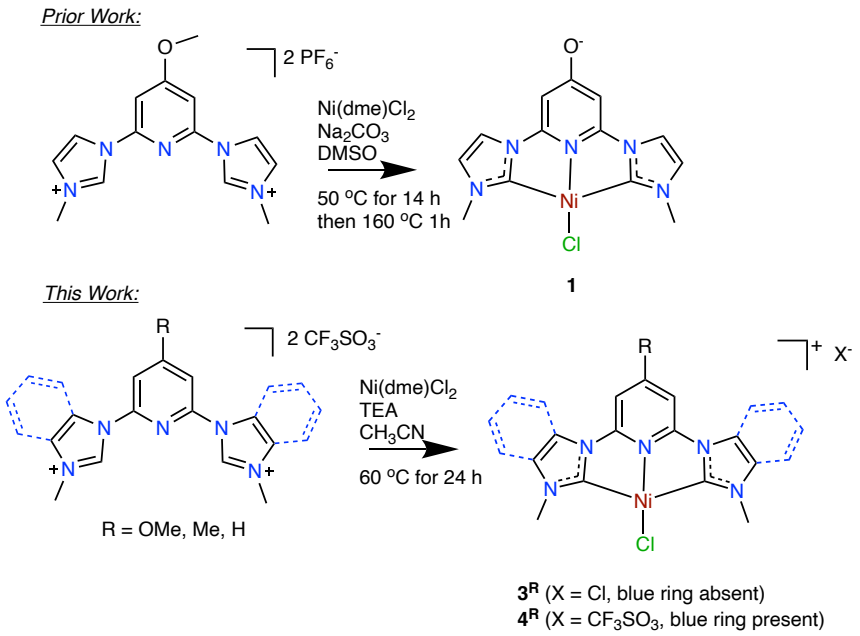

Scheme 1: Synthetic procedure used in 2018 which led to demethylation and the synthetic scheme used herein which left the R groups intact in the synthesis of **3** and **4**.

Crystal Structures

The crystal structures of complexes $\mathbf{3^{OMe}}$, $\mathbf{3^{Me}}$, and $\mathbf{3^{H}}$ are shown in **Figure 2**. These complexes were crystallized by vapor diffusion of diethyl ether into a methanol solution of complex $\mathbf{3^{R}}$. These three complexes contain a CNC pincer featuring an imidazole-derived NHC ring bonded to a pyridine derivative. The 4-coordinate nickel centers have a distorted square planar geometry with τ_4 and τ_4' around 0.1 for all $\mathbf{3^{R}}$ complexes (**Figure 2**). The τ_4 and τ_4' parameters estimate the extent of distortion between square planar (τ_4 and τ_4' = 0) and tetrahedral (τ_4 and τ_4' = 1).[27, 28] The difference between τ_4 and τ_4' is in that the largest angles around the metal center, α and β are treated differently in τ_4' which makes distortions away from ideal tetrahedral geometry more evident. However, for the nearly square planar structures in **Figure 2**, there is very little difference between τ_4 and τ_4' due to similar α and β angles (e.g. α = 179° and β = 162° for $\mathbf{3^{OMe}}$).

The Cl1-Ni1-N3 bond angles in all complexes are near the ideal square planar value of 180º at 178º-179º, but the ∠C-Ni-N bond angles are smaller (e.g. 81º in $\mathbf{3^{OMe}}$) and ∠C-Ni-Cl bond angles are larger than 90° due to the constraints of the chelating pincer ring. The substituents on the *para*-pyridine ring also influence the distance between pyridine and the R group. The bond length of C6-O1 in $\mathbf{3^{OMe}}$ is 1.337(2) Å which reflects partial double bond character due to resonance, as is common for methoxy substituted pincers.[26, 29-31] This result suggests that the OMe group is a π-electron donor. We were not able to obtain crystal structures for the complexes $\mathbf{4^{R}}$ due to their limited solubility in organic solvents.

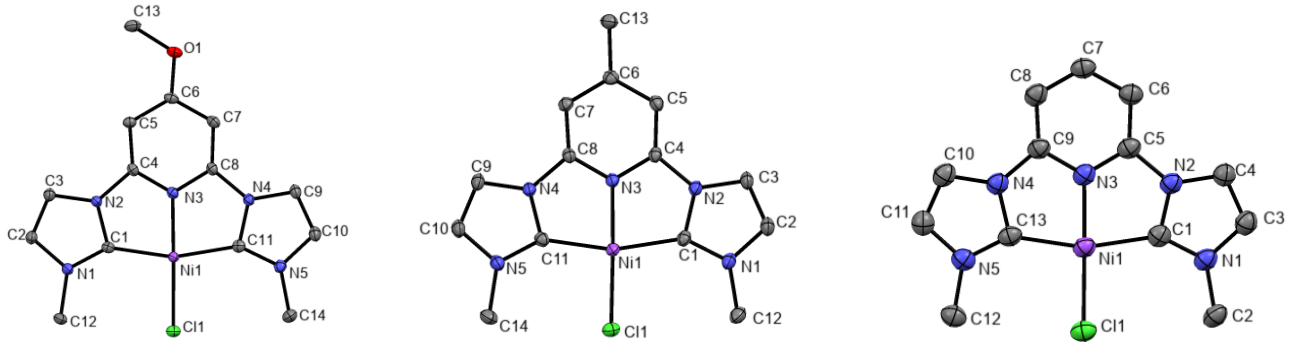

$\mathbf{3^{OMe}}$ $\mathbf{3^{Me}}$ $\mathbf{3^{H}}$

$\tau_4 = 0.13$ $\tau_4 = 0.13$ $\tau_4 = 0.13$
$\tau_4' = 0.07$ $\tau_4' = 0.08$ $\tau_4' = 0.08$

Figure 2: Molecular diagram of the nickel (II) complexes based on crystallographic data with counter anion (Cl^-), solvent molecules and hydrogen atoms removed in all cases for clarity. The τ_4 and τ_4' parameters are also shown. Thermal ellipsoids are drawn at the 50% probability level.

UV-Visible Absorption Spectroscopy

UV-Visible spectroscopy studies were performed to analyze the electronic influence of R substituents in the series of nickel complexes in acetonitrile (**Figure 3**). All complexes show high energy absorptions below 250 nm with high intensity which are assigned to π to π* transitions. The intensity of this band for the benzimidazole-derived NHC ligand is higher than that of the imidazole-derived ligand, due to increased π conjugation. Moderately intense bands are shown between 250 nm and 400 nm for all complexes which are assigned to be metal-to-ligand charge transfer (MLCT). Time dependent density functional theory (TDDFT) computations were performed to provide an understanding of the transition character in the UV-Vis experiments. A comparison with experimental data is needed to calibrate the computational methodology to ensure that reliable comparisons can be made and to substantiate the transition assignments. The simulated spectra performed at the SMD-B3LYP-D3/def2TZVP//B3LYP-D3/BS1 level theory tend to overestimate the experimentally observed absorption energy (**Table S11**). However, the absorption energy trend was found to be consistent with the experimental data showing a linear correlation with $R^2 = 0.97$ (**Figure S56**). Thus, these results can be used to further study the absorption excitation character. A NTO (Natural Transition Orbital) analysis supports that complex $\mathbf{3^{OMe}}$ undergoes an MLCT transition at 348 nm which correlates to the experimental result (373 nm). In this transition, an electron in the d_z^2 orbital of nickel excites to the π* orbital on the pyridyl group. The lack of π* contribution from the benzimidazolyl groups in the CNC ligand for series **4** complexes demonstrates that the extended conjugation has little effect on the ligand electron density accepting strength when compared to the imidazolyl CNC ligand. MLCT bands observed around 370 nm to 385 nm for the other complexes have similar features (see NTO analysis in **Table S6**). The strong donor substituent leads to a shift to shorter wavelength of the

MLCT band which was observed in both experiment and computation. Moreover, complexes $\mathbf{4}^{\mathbf{OMe}}$, $\mathbf{4}^{\mathbf{Me}}$, and $\mathbf{4}^{\mathbf{H}}$ have weak bands above 400 nm (inset, **Figure 3**) which probably involve *d-d* transitions.

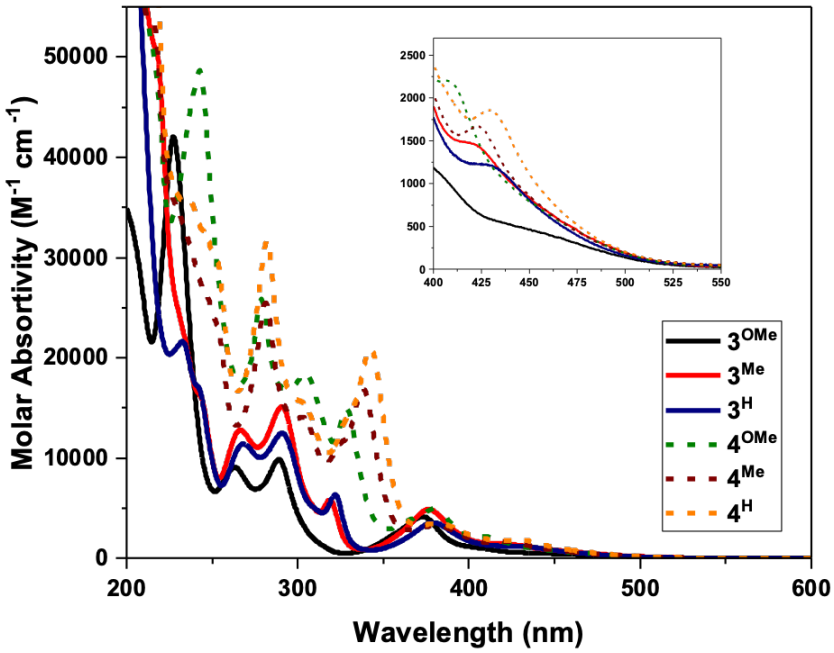

Figure 3: UV-Vis absorption spectra for each complex in acetonitrile at concentration of 0.03 mM. The inset shows an expansion of the region above 400 nm.

Excited State Processes

Photoinduced processes within these six nickel complexes were analyzed using transient absorption (TA) spectroscopy. All six complexes exhibit similar TA spectral features (**Figures S38-S42**); therefore, a global analysis via single value decomposition[32, 33] was performed $\mathbf{3}^{\mathbf{OMe}}$ as a typical example. These results are shown in **Figure 4** and are further discussed in reference to excited-state energy calculations shown in **Figure 5**. Within this figure, notations S_0 and S_1 represent the singlet ground state and the first minimum of the singlet excited state, respectively.

T_1, T_2, and T_3 represent the first, second, and third local minima of the triplet excited states, respectively. The initial UV excitation yields the formation

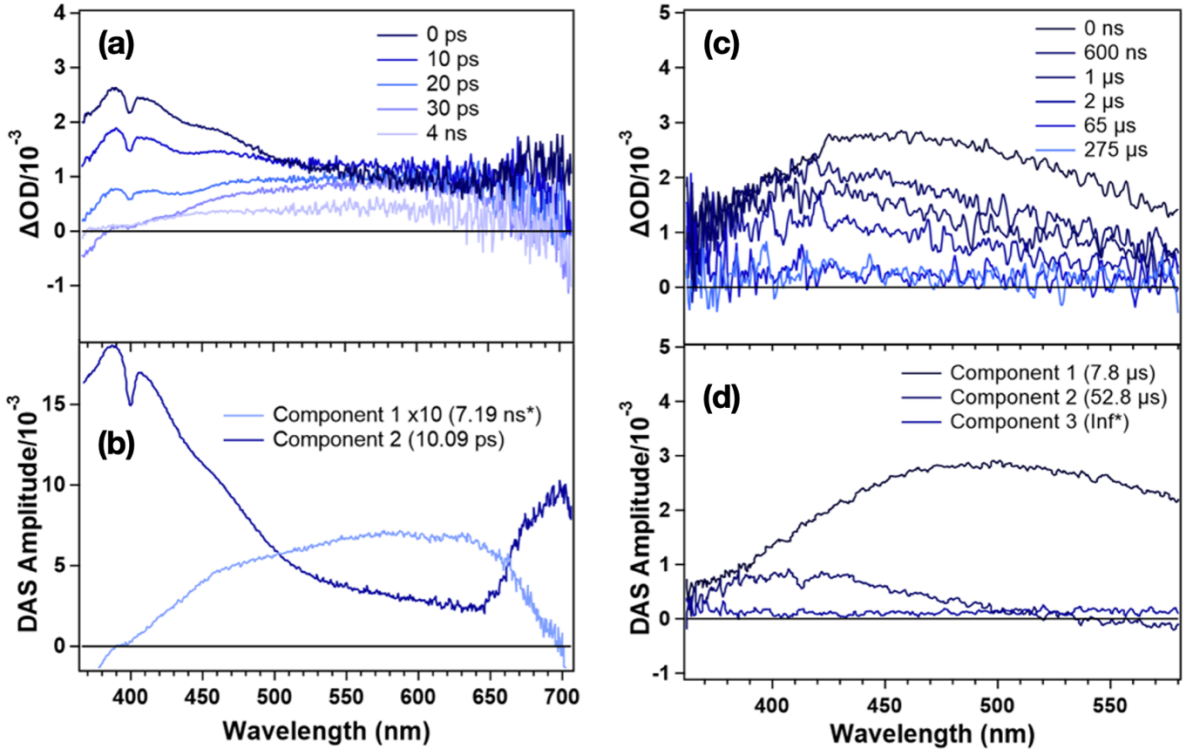

Figure 4. Transient absorption spectra (a, c) and decay associated spectra (DAS, b, d) for the $\mathbf{3^{OMe}}$ complex in the ultrafast (a, b) and nanosecond (c, d) time regimes.

of a singlet metal-to-ligand charge transfer excited state (^{1}MLCT) with an excited state absorption at approximately 400 nm (i.e., Component 2 in **Figure 4b**) that decays in 10.09 ps. The subsequent long lived transients and assignments of related nickel complexes,[21, 22] suggest that the complex then undergoes intersystem crossing (ISC) to the triplet ligand-to-metal charge transfer state (^{3}LMCT) with an excited state absorption centered at 525 nm (**Figure 4b**). Additionally, the computed ^{1}MLCT transition occurring within the vertical excitation from the ground state S_0 is at 82.2 kcal/mol, which closely aligns with the energy level of ^{3}LMCT corresponding to T_2 minimum.

The similarity in energy and the LUTO (lowest unoccupied transition orbital) character further support the validity of ISC occurring within these electronic states. This 525 nm

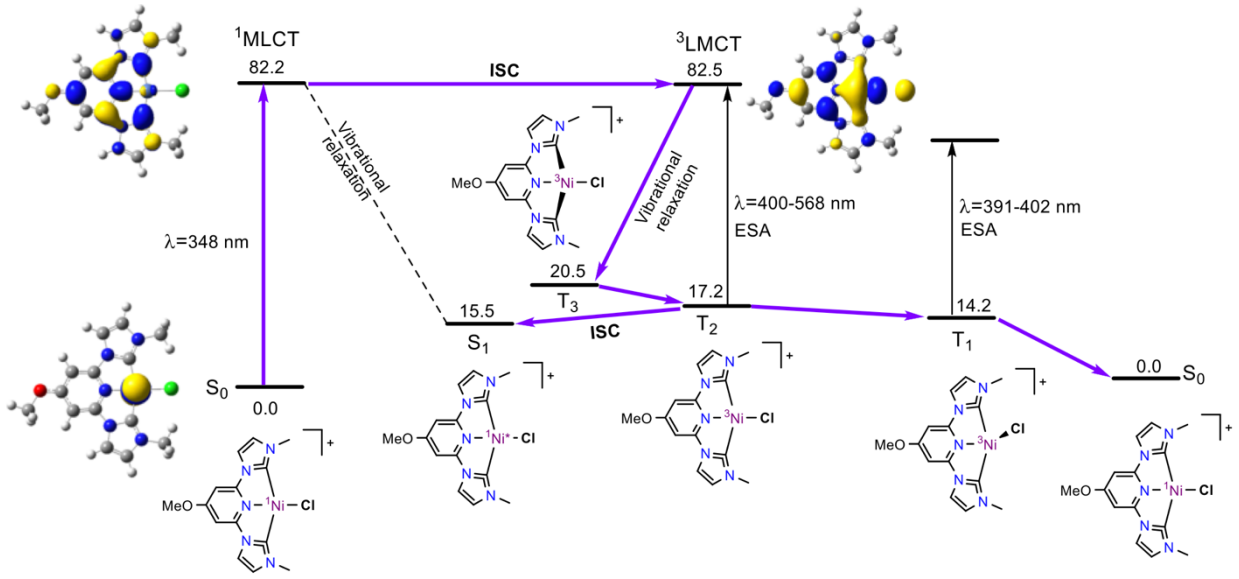

Figure 5. Photophysical energy diagram of $\mathbf{3^{OMe}}$ complex calculated at SMD(MeCN)-B3LYP-D3/def2-TZVP//BS1 level theory. Values listed without units are in kcal/mol.

broadband transient absorption is attributed to d-d transitions within the now formally reduced nickel center, in agreement with work performed on similar complexes.[21, 22] Global analysis yields a decay time constant of 7.2 ns for this state. This value is longer than the lifetimes obtainable by our instrumentation, and the transient of the d-d transitions do not fully decay, indicating that this state lives longer than 7.2 ns.

The earliest time slices in the nanosecond TAS experiments (**Figure 4b**) exhibit an excited state absorption (ESA) at ~500 nm. This experimental result appears to be consistent with the absorption band of T_2, which was predicted to lie in the range of 400-568 nm (**Figure 5** and **Table S15**) through DFT calculations. The data indicates that following intersystem crossing to the ^{3}LMCT state, the photo-pathway (indicated by the purple arrow in **Figure 5**) relaxes to the T_2

minimum. However, it remains inconclusive whether the relaxation from the ^{3}LMCT state to T_2 occurs directly or involves intermediates like T_3 during the process. The state corresponding to T_2 decay was observed to have a transient feature which shifts to higher energy at ~425 nm. This shift can be attributed to relaxation from the triplet minimum of T_2 to T_1 and consequently an increase in the excitation energy. Consistent with these trends, DFT results demonstrate that the ^{3}LMCT transitions of T_2 are at 438 and 431 nm (**Table S15**) and upon population of the ^{3}LMCT of T_1 there is a shift to a shorter wavelength of ~402 nm (see details of the NTO analysis in **Table S16**). In terms of geometry, T_2 exhibits a square planar geometry while T_1 geometry is distorted away from a square planar structure with the chloride ligand out of the plane of the pincer ligand. The geometry change during decay, especially in the case of T_2 to T_1, compared to electronic relaxation, could contribute to the long-lived excited species of these nickel complexes. It is also important to note that S_1 and T_2 geometries are almost identical. A single point calculation on the S_1 geometry with a triplet wave function provides a very close energy to the T_2 local minimum (17.5 vs 17.2 kcal/mol). These results indicate the potential for intersystem crossing (ISC) or reverse intersystem crossing (RISC) between S_1 and T_2 states, and the possibility of two potential decay pathways. In an attempt to extract a comparative lifetime for this decay from either the triplet or singlet state, the final Component 3 was fit with a time constant having an infinite amplitude as the transients do not fully decay within the 450 μs time window.

Single wavelength kinetics of the long-lived state for each complex were fit with either single exponential decay functions with an infinite amplitude component or double exponential decay functions, and the results are summarized in **Table 2** (see **Figures S43 – S48** for fits and parameters). These decay constants yield a comparative metric for the overall decay of this long-lived state. *Note that, as complexes* $\boldsymbol{3^{OMe}}$ *and* $\boldsymbol{4^{OMe}}$ *were fit with infinite amplitudes, these lifetimes*

are actually much longer than what is tabulated below. All six complexes have excited state lifetimes in the microsecond regime (see **Table 2**), which are favorable for bimolecular photochemical processes. As seen in the fit parameters, the error and residuals within these fits is somewhat large at early ns time delays, prohibiting an accurate comparison from being made between the substituent groups. Interestingly, however, introducing an inductive π-donor to either complex (**3**^{OMe} and **4**^{OMe}) leads to a drastic increase in the excited state lifetime, causing both complexes to show transient signals longer than is trackable by the detector. To ensure these exceptionally long lifetimes are not a product of photodegradation, absorption spectra were acquired before and after scans for all complexes (for example, **Figure S49**). The inductive π-donor causing this increase in lifetime is similar to what is seen in our previous work with a ruthenium complex containing a similar ligand having a millisecond lifetime under similar conditions.[34] These exceptionally long lifetimes show the potential for these complexes to effectively drive bimolecular photocatalysis and their promise as CO_2 reductants.

Table 2: Excited state lifetimes of all complexes from exponential fits of the nanosecond transient absorption data. Kinetics were taken from the λ_{max} of the longest-lived transient feature.

Complex	Excited State Lifetime (τ)
3^{H}	2.76 μs
3^{Me}	2.28 μs
3^{OMe}	1.21 μs*
4^{H}	3.50 μs
4^{Me}	1.16 μs

4^{OMe}	1.39 μs*

*These kinetics outlive the lifetime of the detector and were fit with an infinite amplitude applied to the exponential decay function.

Electrochemistry

An electrochemical study was conducted on the six nickel CNC-pincer complexes using cyclic voltammetry (CV) under N_2 and CO_2 atmospheres in acetonitrile solution. This allows us to determine the ability of these nickel complexes to reduce CO_2 electrochemically as well as the thermodynamics related to photocatalytic reduction of CO_2. All complexes undergo multiple reductions under both conditions (CO_2 and N_2) as shown in **Figure S33** and **Table 3**. The first reduction peak (E_{pc1}) of all complexes is observed from -1.1 V to -1.5 V under N_2 and CO_2 (**Table 3**). The addition of extra chloride via the electrolyte results in E_{pc1} not being observed for $\mathbf{3^{Me}}$ and $\mathbf{4^{H}}$ (**Scheme 2** and **Figures S34-S35**). Reduction potentials for all complexes are irreversible, except for the second reductions (E_{pc2}) under N_2 which show a small return peak in some cases (e.g. for $\mathbf{3^{Me}}$ under N_2, see **Figure S33** and see **Figure S35** with peaks labeled for $\mathbf{3^{Me}}$ and $\mathbf{4^{Me}}$). The catalytic current enhancement of CO_2 reduction occurs for E_{pc2} with small i_{cat}/i_p values for all complexes. The reduction potential onset values for E_{pc2} under CO_2 are more positive than $Ir(ppy)_3$, (-2.61 V)[22] as shown in **Table 4** and **Figure 6**. This indicates that $Ir(ppy)_3$ is a suitable PS to drive photosensitized reactions thermodynamically with these Ni complexes. Similar to the nickel complexes **1** and **2** (**Figure 1**), the second onset reduction potentials of complexes $\mathbf{3^{OMe}}$, $\mathbf{3^{Me}}$, and $\mathbf{3^{H}}$ under CO_2 were observed between –1.88 to –2.05 V (**Table 4**).

Overpotentials for CO and formate formation were defined as follows. We assume a pK_a value of 18.5 for protonated triethylamine (the strongest acid under photocatalysis conditions in

acetonitrile[35, 36]) and a standard reduction potential of CO_2 in MeCN at –0.12 V vs. Fc^+/Fc (ferrocenium/ferrocene)[37] which produces a standard reduction potential of CO_2 to form CO under photocatalysis conditions of -1.21 V vs. Fc^+/Fc.[37, 38] Similarly, this yields a standard reduction potential of -1.33 V for conversion of CO to formate.[39] Overpotentials for both products (CO and formate) are shown in **Table 4** and range of 0.23 to 0.84 V. The onset values (-1.88 to -2.05 V) for $\mathbf{3^R}$ are more negative than for the more conjugated nickel complexes with benzimidazole derived NHC rings (-1.56 to -1.74 V for $\mathbf{4^R}$), which reflects the fact that $\mathbf{4^R}$ complexes have lower lying LUMO orbitals (vs. the corresponding $\mathbf{3^R}$ complex) and are easier to reduce. With both the **3** and the **4** series, these values become more negative as R goes from H to Me to OMe, reflecting that the more electron rich substituents are harder to reduce.

Table 3: Reduction potentials (under N_2 and CO_2) for all complexes (Scan rate = 100 mV/s). The variation in the supporting electrolyte was done to probe the role of chloride in this reaction.

Complex	**Reduction Potentials in (V vs Fc^+/Fc) Under N_2 | Under CO_2 (i_{cat}/i_p)**				
	E_{pc1}	E_{pc2}	E_{pc3}	E_{pc4}	Supporting Electrolyte
$\mathbf{3^{OMe}}$	-1.44 | -1.45	-2.20 | - 2.22 (2.33)	n/a	n/a | -2.64	$TBAPF_6$
	-1.64 | -1.71	-2.17 | -2.07	n/a	n/a | -2.68	TBACl
$\mathbf{3^{Me}}$	-1.38 | -1.39	-2.02 | -2.00 (1.29)	n/a | -2.29	n/a | -2.72	$TBAPF_6$
	n/a*	-2.05 | - 2.04	n/a	-2.53 | -2.68	TBACl
$\mathbf{3^H}$	- 1.47 | -1.40	-2.04 | -1.97	n/a	n/a | -2.73	$TBAPF_6$

		(1.29)			
	-1.53 | -1.58	n/a | -1.89	n/a	-2.38 | -2.55	TBACl
4^{OMe}	-1.20 | -1.20	-1.85 | -1.80 (1.32)	n/a | -2.21	n/a	$TBAPF_6$
	-1.37 | -1.36	-1.61 | -1.73	n/a	-2.48| -2.68	TBACl
4^{Me}	-1.34 | -1.35	-1.8 | -2.1 (2.26)	n/a	n/a | -2.71	$TBAPF_6$
	-1.57 | -1.67	n/a | -1.99	n/a	-2.40 | -2.62	TBACl
4^{H}	-1.17 | -1.16	-1.73 | -1.60 (1.15)	n/a | -2.01	n/a | -2.75	$TBAPF_6$
	n/a*	-1.91 | n/a*	n/a	-2.34 | -2.58	TBACl

*the E_{pc} of these peaks are not obvious so the reduction potentials could not be determined.

The cyclic voltammetry studies reveal that, under CO_2, complex **3^{Me}**, **4^{OMe}**, and **4^{H}** exhibit four reduction events with the tetrabutylammonium hexafluorophosphate ($TBAPF_6$) electrolyte denoted as E_{pc1}, E_{pc2}, E_{pc3}, and E_{pc4}. These events are listed in the order of decreasing reduction potential and grouped together to describe the specific electrochemical events (**Table 3**, **Scheme 2**, and **Figure S35**). Meanwhile the other three complexes **3^{OMe}**, **3^{H}**, and **4^{Me}** display only three reduction events, lacking an event analogous to E_{pc3}, perhaps due to decomposition of intermediates formed prior to E_{pc3}. Interestingly, based on DFT computations (**Table S9**), it is more difficult for these complexes to lose halide compared to the remaining complexes. These results suggest a potential connection between the absence of E_{pc3} and the halide dissociation (or re-coordination) process.

Table 4: Further electrochemical data for E_{pc2} for catalytic CO_2 reduction to form CO with various nickel(II) complexes.[a]

Complex	E_{pc2} Peak N_2/CO_2 (V)	E_{pc2} Onset N_2/CO_2 (V)	Overpotential for CO (V)	Overpotential for HCO_2^- (V)	i_{cat}/i_p
$\mathbf{3^{OMe}}$	-2.20/-2.22	-2.06/-2.05	0.84	0.72	2.33
$\mathbf{3^{Me}}$	-2.02/-2.00	-1.97/-1.96	0.75	0.63	1.29
$\mathbf{3^{H}}$	-2.04/-1.97	-1.91/-1.88	0.67	0.55	1.29
$\mathbf{4^{OMe}}$	-1.85/-1.80	-1.81/-1.74	0.53	0.41	1.32
$\mathbf{4^{Me}}$	-1.81/-2.1	-1.76/-1.70	0.49	0.37	2.26
$\mathbf{4^{H}}$	-1.73/-1.60	-1.69/-1.56	0.35	0.23	1.15

[a]Reduction potentials are given against Fc^+/Fc.

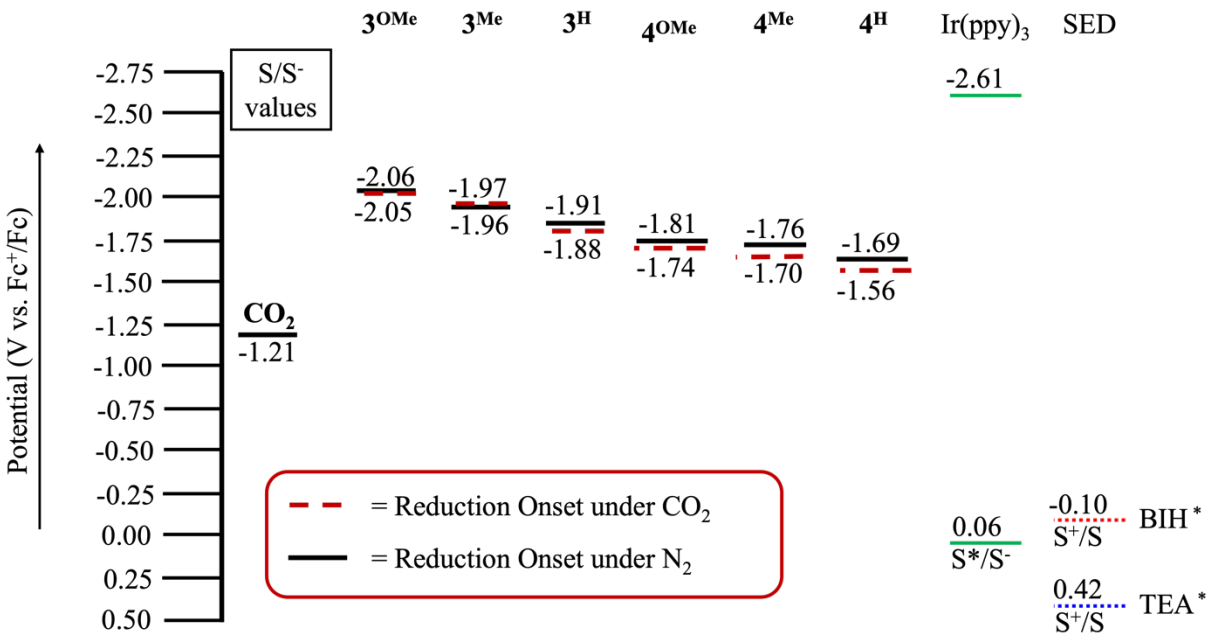

Figure 6: Energy level diagrams based on onset potential for E_{pc2} of the catalyst (Table 4), PS (CV and optical data), and sacrificial electron donors (SEDs) in acetonitrile. Solid lines are estimated reduction onset potentials for E_{pc2} under inert atmosphere, dashed are the reduction onset potentials for E_{pc2} under CO_2, and short dashes are oxidation potentials. TEA is triethylamine; BIH is shown in **Figure 1**. *BIH and TEA are onset values.[40]

The electrochemical events observed by cyclic voltammetry are proposed in **Scheme 2** and involve several steps: multiple electron transfer events, halide dissociation, CO_2 coordination, and protonation.[41, 42] Thus, it appears that one electron is used to activate the complexes and two electrons are used to drive electrochemical CO_2 reduction. Initial electron transfer to $^{1}[LNi^{II}\text{-}Cl]^{+}$ produces $^{2}[LNi^{I}\text{-}Cl]$ which can then undergo chloride loss to form $^{2}[LNi^{I}]^{+}$. This activation process can occur either through a step-wise mechanism E/C or a concerted EC step[42] as shown in **Scheme 2**; this is tentatively assigned as E_{pc1} (see **Table S8**). The stepwise and concerted mechanisms are close in energy to each other and cannot be distinguished computationally (**Table S9**). E_{pc2} and

E_{pc3} are likely to correspond to reduction events involving CO_2-bound to Ni species on the pathway to the production of CO and/or formate. For example, E_{pc2} may correspond to the reduction of a $^2[LNi^ICO]^+$ species to Ni^0 (see **Figure S54** and **Table S10**), however other Ni(I) species bearing similar neutral ligands in place of CO may be reduced at similar potentials. Assigning these events explicitly presents challenges due to the irreversible multiple electrochemical process and inconsistent behavior in control experiments (**Figure S35**). E_{pc3} can be tentatively assigned to the reduction of $^1[LNi^{II}COOH]^+$ (see **Figure S55**). The E_{pc3} event is only observed in certain complexes ($\mathbf{3^{Me}}$, $\mathbf{4^{OMe}}$, and $\mathbf{4^H}$). Inhibition of chloride loss or interception of intermediates by added external chloride (via TBACl as the electrolyte, **Table 3, Figure S34**) appears to prevent observation of E_{pc3} ($\mathbf{3^{Me}}$, $\mathbf{4^{OMe}}$, and $\mathbf{4^H}$) processes. Lastly, E_{pc4} occurs at very negative potentials (-2.55 to -2.75 V under CO_2) and may correspond to the reduction of a "naked" $[LNi^I]$ species to Ni^0 (see **Table S10**). While we acknowledge that CV experiments may not capture all the mechanistic details of the catalytic process, these results still provide insightful information that is consistent with our studies of the photocatalytic CO_2 reduction by experimental and computational methods (*vide infra*).

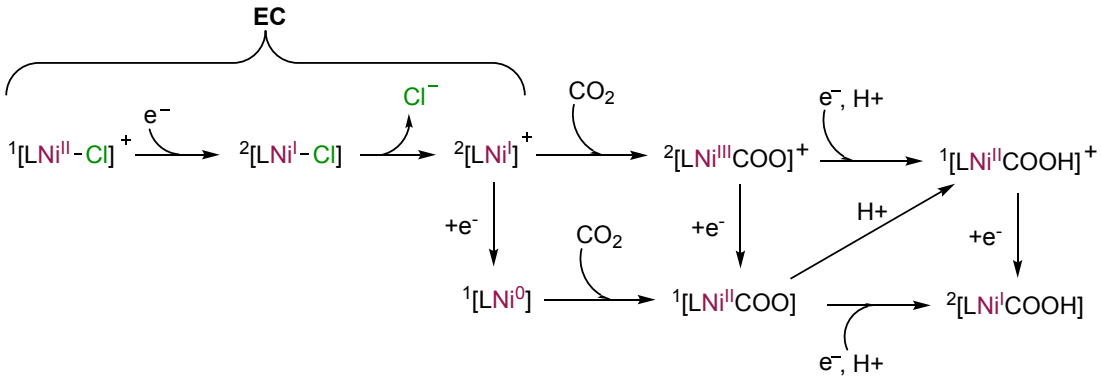

Scheme 2: Proposed mechanism for cyclic voltammetry events. These CO_2 bound products can undergo further reduction and protonation leading to the products CO and formate.

Photocatalytic CO_2 Reduction

The nickel complexes were evaluated in the photocatalytic CO_2 reduction reaction using $Ir(ppy)_3$ as a strongly reducing (-2.61 V vs Fc^+/Fc) photosensitizer (PS).[40] The sacrificial donor BIH was used due to its strong reducing ability. Triethylamine (TEA) was added primarily to serve as a base to deprotonate the BIH cation formed after electron transfer to the PS to promote an irreversible electron transfer event.[40] Photocatalytic reactions in this study were performed in anhydrous acetonitrile with 1 μM catalysts concentration, 1×10^{-4} M of $Ir(ppy)_3$, 0.01 M of BIH as sacrificial electron donor, and 0.36 M of TEA. Upon irradiation of this mixture, the turnover number (TON; moles of product (CO, H_2, CH_4, or HCO_2^-)/moles of Ni catalyst) for each catalyst was determined at 72 h based upon practical considerations given that the catalysts were still actively producing CO at this time point (see **Table 5**, the TOF_F column for the final TOF values measured between 48 and 72 h). Additionally, the turnover frequency (TOF = TON/reaction time) is monitored at various time points. In general, all catalysts produced primarily HCO_2^- (formate) with appreciable CO. Only low to trace amounts of H_2 and CH_4 were detected (**Table S17**). Because CO is a gas that can be monitored with small headspace samples via gas chromatography, continuous monitoring of this product was conducted. Monitoring formate requires using a significant portion of the reaction mixture for ^1H NMR spectroscopy and was therefore monitored at 72 h only.

The turnover number of CO (TON_{CO}) values varied from 516 to 695 under $Ir(ppy)_3$ photosensitized conditions (**Figure 7**, **Table 5**). Overall, the trend for observed TON_{CO} at 72 h is as follows: $\mathbf{4^{Me}} \geq \mathbf{3^{H}} \geq [\mathbf{4^{H}} \simeq \mathbf{4^{OMe}}] \geq [\mathbf{3^{OMe}} \simeq \mathbf{3^{Me}}]$ with bracketed catalysts having TON values within experimental error of each other. The initial TOF_{CO} values (TOF_I) show a trend as follows:

$\mathbf{3^{Me}}$ > [$\mathbf{4^{Me}} \simeq \mathbf{4^{OMe}} \simeq \mathbf{3^{OMe}}$] > [$\mathbf{3^{H}} \simeq \mathbf{4^{H}}$], with $\mathbf{3^{H}}$ and $\mathbf{4^{H}}$ being inactive initially. The TOF_I trend suggests the R group plays an important role in the initial CO production, where the Me group shows higher TOF_I, followed by OMe, and lastly H. The maximum TOF values (TOF_M), however, are similar across the imidazole and benzimidazole derived complexes, which suggests a similar rate of reactivity in the catalytic cycle. This suggests the active catalyst is more rapidly accessed with higher turnover numbers with Me as the R groups (shown by TOF_I), but all catalysts have comparable rates once the active species are available (shown by TOF_M). The most robust catalyst is $\mathbf{4^{Me}}$ which also bears a methyl R group. These catalysts exhibit quantum efficiencies (Φ_{CO}) of ~10^{-3} % which are comparable to other first row metal photocatalysts in bimolecular (PS and catalysts) driven reactions (**Table 5**).[8, 14, 43] CO production rates across the series appear to follow a similar increase leading up to 48 h. After 48 h, three of the catalysts decrease significantly in rate.

Table 5. Photocatalytic results of CO production by nickel complexes $\mathbf{3^{R}}$ and $\mathbf{4^{R}}$ in the presence of $Ir(ppy)_3$ as a photosensitizer. All experiments were performed in duplicate or triplicate.

Complex	TON_{HCO2-} [a]	TON_{CO}[a]	TOF_I $[h^{-1}]$[b]	TOF_M $[h^{-1}]$[c]	TOF_F $[h^{-1}]$[d]	Φ_{CO} (%)
$\mathbf{3^{OMe}}$	2848 ± 86	550 ± 21	1.38	11.21	2.36	$2.54x10^{-3}$
$\mathbf{3^{Me}}$	3217 ± 587	516 ± 53	3.92	12.33	0.92	$2.90x10^{-3}$
$\mathbf{3^{H}}$	2808 ± 58	630 ± 76	0.0	11.60	7.85	$2.45x10^{-3}$
$\mathbf{4^{OMe}}$	2467 ± 745	575 ± 62	1.41	12.85	1.29	$3.04x10^{-3}$
$\mathbf{4^{Me}}$	3445 ± 229	695 ± 18	1.50	11.60	7.91	$2.79x10^{-3}$
$\mathbf{4^{H}}$	2154 ± 323	584 ± 22	0.0	10.66	4.97	$2.45x10^{-3}$

[a]TON values were measured at 72 h. [b]Initial TOF values are reported at 1 h for CO production. [c]TOF_{max} values are given for the time point with the fastest rate of reaction for CO production. [d]TOF final was measured between 48h and 72 h for CO production.

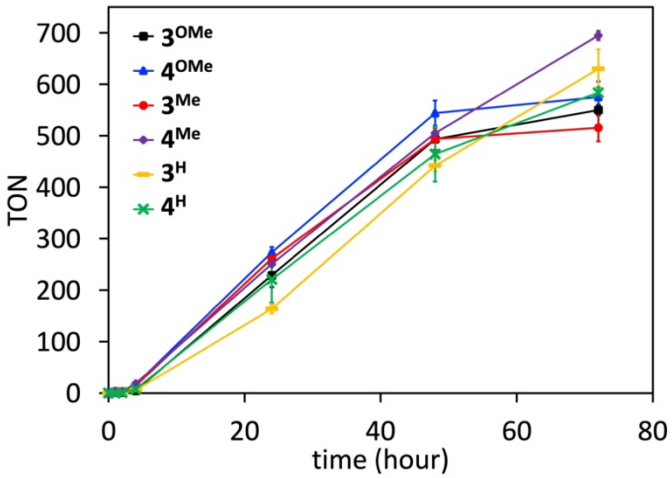

Figure 7. TON versus time plot for the photocatalytic reduction of CO_2 in the presence of $Ir(ppy)_3$ with error bars calculated from a standard deviation of 2-3 runs.

Each catalyst was also analyzed for the production of HCO_2^- (**Table 5**). The production of HCO_2^- was calculated via ^1H NMR (**Figures S57-S68**) once the reactions were stopped at 72 h following literature procedure (details found on pg. **S63**).[40, 44] Interestingly, HCO_2^- was produced by all the catalysts as the primary product from the CO_2 reduction reaction in roughly 4-5 fold larger amounts than CO. Electrocatalytically, Ni catalysts are reported to produce formate in the literature; however, CO is the more common product especially in photocatalysis.[45] The trend for TON_{HCO2-} is [$\mathbf{4^{Me} \simeq 3^{Me}}$] > [$\mathbf{3^{OMe} \simeq 3^{H}}$] > [$\mathbf{4^{OMe} \simeq 4^{H}}$] which varies significantly from the TON trend for CO production. Catalyst $\mathbf{3^{Me}}$ most notably shows a much higher relative yield for formate over CO. It is important to note, however, that replacing the CO_2 atmosphere with N_2 or removing the Ni complex from the reaction as negative controls resulted in no appreciable CO formation (**Table S4**).

Given the reasonably long microsecond excited-state lifetimes observed via transient absorption spectroscopy with the Ni-complexes (*vide supra*), it is plausible that the Ni complex serves as the photocatalyst. To investigate this possibility, $Ir(ppy)_3$ was excluded from the reaction conditions. This experiment was done to assess whether the Ni complexes are capable of absorbing light, being reductively quenched in the excited state by BIH, and driving catalysis. The light absorption and excited state quenching steps are unique to the self-sensitized system and thus no correlation to the $Ir(ppy)_3$ sensitized results is necessary. All six complexes in this series of nickel catalysts are found to also be self-sensitized photocatalysts for the CO_2 reduction reaction (**Table 6** and **Figure 8**).

The trend in TON_{CO} for the catalysts in self-sensitized reactions are as follows: $\mathbf{4^{Me}} > \mathbf{4^{H}} > [\mathbf{4^{OMe}} \simeq \mathbf{3^{Me}}] > \mathbf{3^{H}} > \mathbf{3^{OMe}}$. Interestingly, the data suggests that for self-sensitization, the benzimidazole catalysts ($\mathbf{4^{R}}$) reduces CO_2 to CO more effectively as compared to the imidazole-based catalysts ($\mathbf{3^{R}}$). Complex $\mathbf{4^{Me}}$ was yet again found to be the most durable photocatalyst with 86 TON_{CO} within 72 h and no loss of activity was observed before the reaction was stopped at 72 h. Importantly, all the complexes have initial time periods of $\geq$ 4 h where no detectable CO is produced; of course we are unable to measure formate in this time period and we cannot rule out initial formate production. Thus, these complexes are considered pre-catalysts (for CO at least) and may need to be activated to enter the catalytic cycle. The TOF_M are similar across the series ranging from 0.62-1.63 h^{-1} except for $\mathbf{4^{Me}}$ which has the highest TOF_M of 4.15 h^{-1}. The TOF_F values across the series range from 0.19-1.61 h^{-1} with $\mathbf{4^{Me}}$ having the highest value. Quantum efficiencies (Φ_{CO}) of ~10^{-4} % (**Table 6**) are an order of magnitude lower than in the photosensitized system (**Table 5**). These low values may suggest inefficient light harvesting or catalyst decomposition events; however, we stress that photocatalytic self-sensitized mononuclear Ni catalysts are rare.

Each catalyst was also analyzed for the production of HCO_2^- (**Table 6**). Again, minimal H_2 and CH_4 is produced in the reaction with HCO_2^- being the primary product formed (**Table S18**). Catalyst $\mathbf{4^{Me}}$ ranks the highest in production of HCO_2^- and CO, both in the sensitized and self-sensitized reactions. The formate concentration was calculated via ^{1}H NMR once the reactions were stopped at 72 h (**Figures S69-S81**). The trend for HCO_2^- production shows $\mathbf{4^{Me}}$ >> [$\mathbf{4^{OMe}} \simeq \mathbf{3^{H}} \simeq \mathbf{3^{Me}} \simeq \mathbf{4^{H}}$] >> $\mathbf{3^{OMe}}$ which does not show a clear trend with respect to R groups on the catalyst or imidazole vs. benzimidazole based ligands. Catalyst $\mathbf{4^{Me}}$ produces the most HCO_2^- out of the series at a value of 965 with $\mathbf{3^{OMe}}$ producing the least at 357, and the other catalysts lying in a similar range between 584-633. Importantly, each of these catalysts produce a significant amount of HCO_2^- through self-sensitized photocatalysis. Literature precedence suggests the addition of a proton source in photocatalytic reactions may lead to an increase in catalytic activity and product formation.[46] Three proton sources (water, trifluoroethanol (TFE), and PhOH) were added at a 0.50 M concentration (**Table S19, Figures S87-88**). Surprisingly, the addition of water and TFE to the reactions led to no product formation, while the addition of PhOH led to some product formation but with a large decrease in TON (**Table S19, Figures S87-88**). This contrasts with some literature photocatalytic studies, especially in the use of phenol as a proton source.[47, 48] The balanced chemical equation for production of formate requires 2 H^+ for every 1 equivalent of HCOOH or HCO_2^- produced. However, even for $\mathbf{4^{Me}}$ (TON = 965), this would only require ~2 mM of an H^+ source based upon stoichiometry. This may indicate that protonation of a Ni catalytic intermediate leads to decomposition of the catalyst, and perhaps future studies should investigate lower quantities of H^+ sources or acids of varied pK_a values. We note that TEA is present in all our reactions to deprotonate the BIH derived radical cation, and the addition of a proton source may be disruptive to catalysis reliant on a BIH/TEA based electron/proton transfer system.

Catalyst $\mathbf{4^{Me}}$ across all measurements proved to be the most efficient, with and without a photosensitizer. Therefore, $\mathbf{4^{Me}}$ was chosen as the catalyst to perform additional experiments to assess the proposed mechanism and check for potential nanoparticle formation and catalytic activity of such particles using dynamic light scattering (DLS) and the mercury (Hg^0) and Maitlis tests, respectively (**Figure S82** & **Table S20**). DLS after photocatalytic CO_2 reduction under typical reaction conditions with $Ir(ppy)_3$ does show nanoparticle formation (**Figure S82**), but further investigations (below) suggests these nanoparticles are not catalytically active. The Hg^0 and Maitlis tests were conducted to observe potential nanoparticle catalytic activity and analyzed for the products of CO_2 reduction: CO, H_2, CH_4, and HCO_2^- (**Table S20**). The mercury test normally involves Hg^0 addition after catalyst initiation, to amalgamate any Ni- or Ir-based nanoparticles; this would therefore lead to decreased activity if such nanoparticles were catalytically active.[14] Excess Hg^0 (0.5 mL) was added after irradiating $\mathbf{4^{Me}}$ for 24 h and this solution shows comparable (within 10%) catalytic reactivity from 24-72 h to that observed without mercury added (**Table S20, Figures S89-90**). Thus, it can be concluded that nanoparticles are being formed (by DLS), but they are not catalytically active. The Maitlis test was also performed after 24 h of irradiation via in-line filtration of the reaction through a pad of celite under a N_2 atmosphere, whereby any nanoparticles formed are removed from the reaction vessel and the reaction is carried forward under CO_2.[49, 50] Similarly, if nanoparticles contribute to the catalytic activity, then a decrease in TON values is expected. The Maitlis test resulted in no appreciable decrease (approximately 1%) in TON_{CO} compared to the control reaction and even an increase in $TON_{HCO2–}$, possibly due to removal of some catalytic cycle inhibitor (**Table S20, Figure S91**). These results suggest that the nanoparticles formed in the reaction do not contribute to catalytic performance and further, the presence of the nanoparticles may even hinder catalytic activity (**Table S20).**

Importantly, these experiments all suggest the true catalysts are molecular since no evidence of nanoparticle-based catalysis was observed.

As mentioned above, the catalysts require activation prior to showing self-sensitized catalytic activity, suggesting three steps are required relative to the photosensitized system: catalyst generation, visible light absorption, and excited state reductive quenching. Furthermore, we speculate based on computational data (below) that active catalyst generation may be key to explaining the mechanism of self-sensitized catalysis.

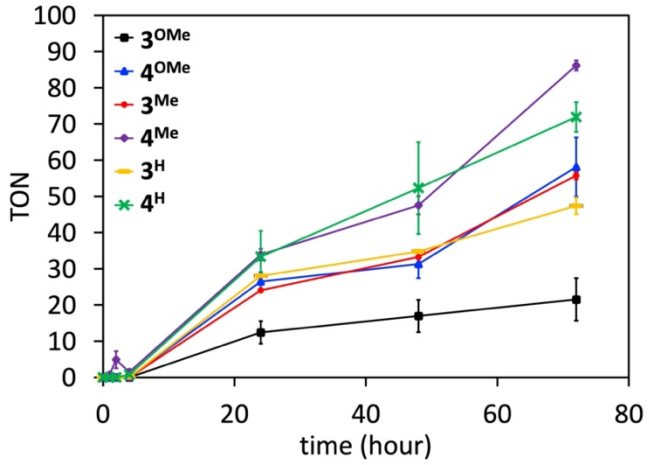

Figure 8. TON versus time plot for the photocatalytic CO_2 reduction reaction with Ni complexes (no added $Ir(ppy)_3$) with error bars calculated from a standard deviation of 2-3 runs.

Table 6. Photocatalytic results of CO production by nickel complexes without the presence of a photosensitizer. All experiments were performed in duplicate or triplicate.

Complex	TON_{HCO2-}[a]	TON_{CO}[a]	TOF_I [h^{-1}][b]	TOF_M [h^{-1}][c]	TOF_F [h^{-1}][d]	Φ_{CO} (%)
$\mathbf{3^{OMe}}$	357 ± 13	22 ± 12	0.0	0.62	0.19	$1.38x10^{-4}$
$\mathbf{3^{Me}}$	629 ± 130	56 ± 2	0.0	1.20	0.94	$2.67x10^{-4}$
$\mathbf{3^{H}}$	633 ± 109	47 ± 5	0.0	1.40	0.52	$3.12x10^{-4}$
$\mathbf{4^{OMe}}$	608 ± 146	58 ± 16	0.0	1.32	1.12	$2.94x10^{-4}$

4^{Me}	965 ± 176	86 ± 3	0.73	4.15	1.61	$6.52x10^{-4}$
4^{H}	584 ± 201	72 ± 8	0.0	1.63	0.82	$2.59x10^{-4}$

[a]Measured at 72 h. [b]Initial TOF values are reported at 1 h for CO production. [c]TOF_{max} values are given for the time point with the fastest rate of reaction for CO production. [d]TOF final was measured between 48 h and 72 h for CO production.

Proposed Mechanistic Steps: The Role of Halide in Formation of the Active Catalyst

The CO_2 reduction could be understood as two parallel processes for sensitized reactions: 1) a sensitizer absorbs light energy and receives electrons and protons from sacrificial donors and 2) a catalytic role of the nickel complex in using those electrons and protons for CO_2 conversion to CO and formate. For the self-sensitized photocatalytic cycle, the nickel complex replaces the role of $Ir(ppy)_3$ in the former process while the latter role is assumed to remain the same. However, the active species corresponding with the production of CO (even in the presence of $Ir(ppy)_3$) are not obvious. Catalyst activation via the loss of the chloride is proposed but does not necessarily rule out catalytic activity of the chloride-bound complex. The DFT computations examining chloride dissociation illustrate that the energy cost is diminished for both the series of triplets $^3[LNi^{II}Cl]^{*+}$ and the one-electron reduced species $^2[LNi^{I}Cl]$ when compared to halide loss from the series of initial $^1[LNi^{II}Cl]^+$ complexes, which demand more energy for chloride loss (**Table S9**, L = CNC pincer). For all complexes, chloride loss from the one-electron reduced species, $^2[LNi^{I}\text{-}Cl]$, is considerably less energy intensive. Specifically, complexes **4^{H}** and **4^{OMe}** have a free energy favored chloride dissociation from the triplet state (Gibbs free energy are exergonic, -3.7 and -3.6 kcal/mol, respectively). Considering the four remaining complexes (**4^{Me}**, **3^{Me}**, **3^{H}**, and **3^{OMe}**), chloride loss from the one-electron reduced species is the least thermodynamically favorable for **3^{H}** and **4^{Me}**.

It is important to note that CO_2 reduction, with or without a photosensitizer (PS), can be facilitated by two different active catalysts. We propose that the $^1[LNi^{II}Cl]$ species is more

photocatalytically active in the self-sensitized reaction, while in the presence of the iridium-based PS, the halide loss product $^{1}[LNi^{0}]$ is required to achieve optimal reactivity (**Figure 9**). We note that **Figure 9** summarizes the calculated reduction potentials for the relevant Ni(II) and Ni(I) excited state species derived from all six complexes, and therefore this figure captures the general trends in both sensitized and self-sensitized reactivity. To assess the probability for halide loss from the active catalyst species, excess chloride salt, 0.1 M NBu_4Cl, was added to the photocatalytic reaction of $\mathbf{4^{Me}}$ with and without the photosensitizer, $Ir(ppy)_3$, present. When NBu_4Cl was added to the reaction with no $Ir(ppy)_3$ present, all products increased significantly, especially CO and HCO_2^- (**Table S19, Figures S83-84**). These results suggest that an excess of Cl ions in the reaction promotes the presence of higher concentrations of the $^{1}[LNi^{II}Cl]^{+}$ species in solution, and this species is efficient at both light harvesting and oxidation of the sacrificial donors via $^{3}[LNi^{II}Cl]^{*+}$ conversion to $^{2}[LNi^{I}Cl]$ (**Figure 9**). This finding is consistent with the relationship between halide complexes and photocatalytic activity, as discussed in the electrochemistry section. Conversely, when $Ir(ppy)_3$ is added to the reaction with $\mathbf{4^{Me}}$, $Ir(ppy)_3$ absorbs the light energy and extracts electrons from the sacrificial donor (rather than the Ni catalysts so the Ni-Cl species is not needed) and the presence of extra halide prevents the formation of the more active species $^{1}[LNi^{0}]$ for reaction with CO_2, thereby decreasing the TON of CO and HCO_2^- (**Table S19**, **Figures S85-86**).

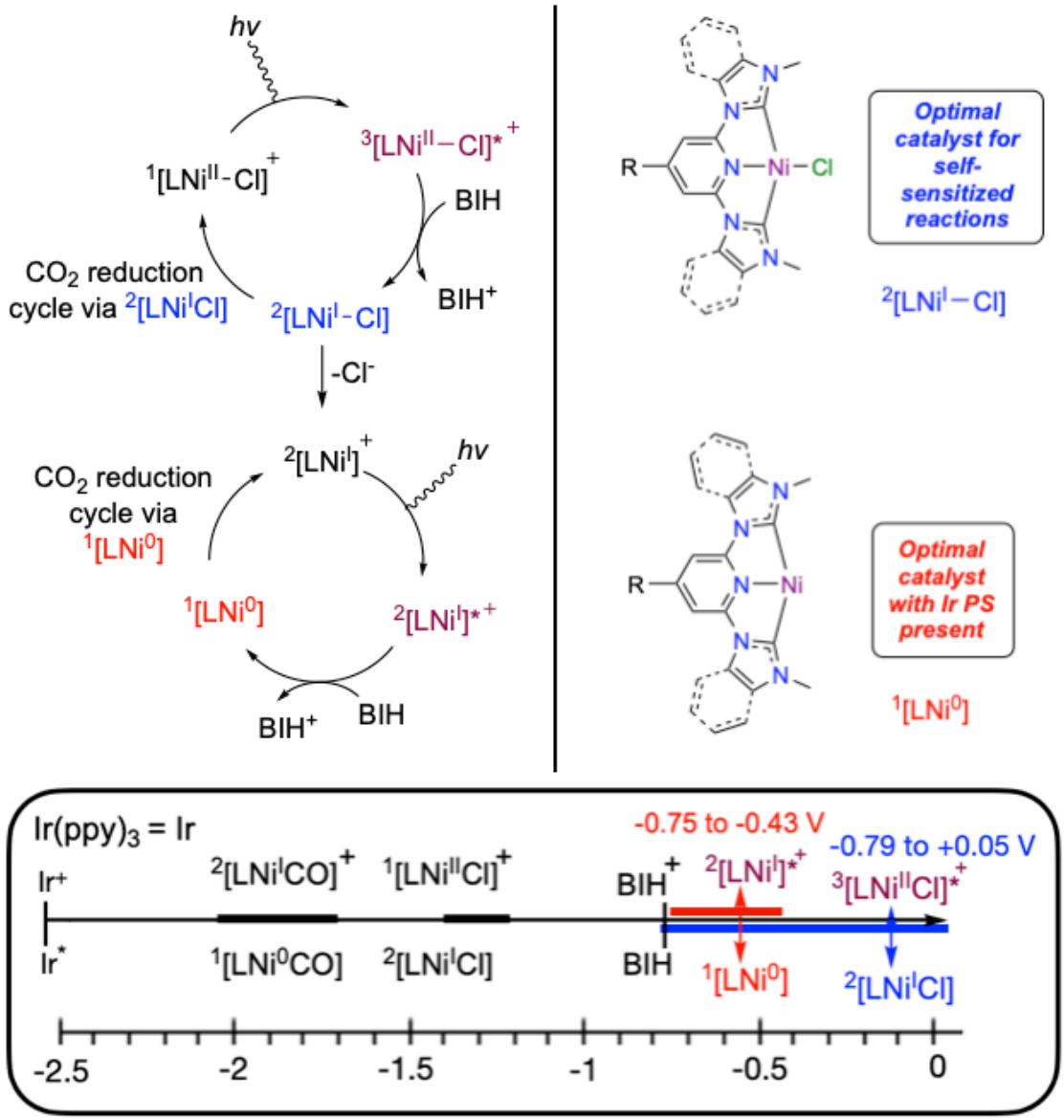

Figure 9. Top: Proposed self-sensitized photocatalytic mechanism showing that while both cycles (via Ni^I in blue or Ni^0 in red) can achieve self-sensitized catalysis, the top cycle has more favorable reduction potentials. **Bottom**: Computed reduction potentials (V) vs Fc^+/Fc. Nickel complexes summarized include derivatives of all six complexes (see Tables S8, S10, and S12). Ground state species are shown in black, red, or blue and excited states are in burgundy.

Proposed Mechanism for CO and Formate Production

Next, we examined the catalytic activity of $^{1}[LNi^{II}Cl]^{+}$ and $^{1}[LNi^{0}]$ species by DFT computations. Catalyst $\mathbf{3^{OMe}}$ is highlighted in **Schemes 3** and **S1** due to our extensive TAS studies of the excited states for this species. The transformation from CO_2 to CO, catalyzed by $^{1}[LNi^{II}Cl]^{+}$ involves the following steps: electron transfer, CO_2 coordination, proton transfer, and PCET (proton coupled electron transfer) (as illustrated in the cycle on the right-hand side of **Scheme S1**). The reduced complex $^{2}[LNi^{1}\text{-}Cl]$ is a key intermediate with the catalytic pathways bifurcating at this point. Intermediate $^{2}[LNi^{1}\text{-}Cl]$ can be protonated to form a hydride which can then insert CO_2 leading to HCO_2^{-} after electron transfer (illustrated in the cycle on the left-hand side of **Scheme S1**). Similar mechanisms catalyzed by $^{1}[LNi^{0}]$ demonstrate significant favorability in analogous chemical steps but require more energy in the electron transfer steps (**Scheme 3**). It is probable that both catalytic species coexist in solution and potentially are accessed by both sensitized and self-sensitized pathways, posing a challenge in analyzing selectivity in each individual process.

The formate ion can be produced from either reduced species ($^{1}[LNi^{0}]$ or $^{2}[LNi^{I}Cl]$ in **Scheme 3** or **S1**, respectively, left-hand circles). The competition between CO vs. formate production is determined by whether Ni^{I} or Ni^{0} coordinates CO_2 versus undergoes protonation at the metal center to form a nickel hydride. The thermodynamic energies of these two competitive steps for $^{2}[LNi^{I}Cl]$ complex are very similar, with $\Delta G = 6.2$ kcal/mol for protonation and $\Delta G = 4.7$ kcal/mol for CO_2 coordination (see **Scheme S1**). However, in the unsaturated species $^{1}[LNi^{0}]$, the analogous transformation would significantly favor hydride formation, with $\Delta G = -62.5$ kcal/mol and $\Delta G = -22.8$ kcal/mol, respectively (**Scheme 3**). The formation of formate as the major product is likely influenced by this difference in energies. In the subsequent step, CO_2 can insert into the nickel hydride to produce bound formate. Electron transfer to nickel the initiates the dissociation

of formate to complete the cycle (**Schemes 3** and **S1**). While these steps were calculated for **3^{OMe}**, we do not anticipate major differences for the other complexes which display similar TON values and similar ratios of formate to CO.

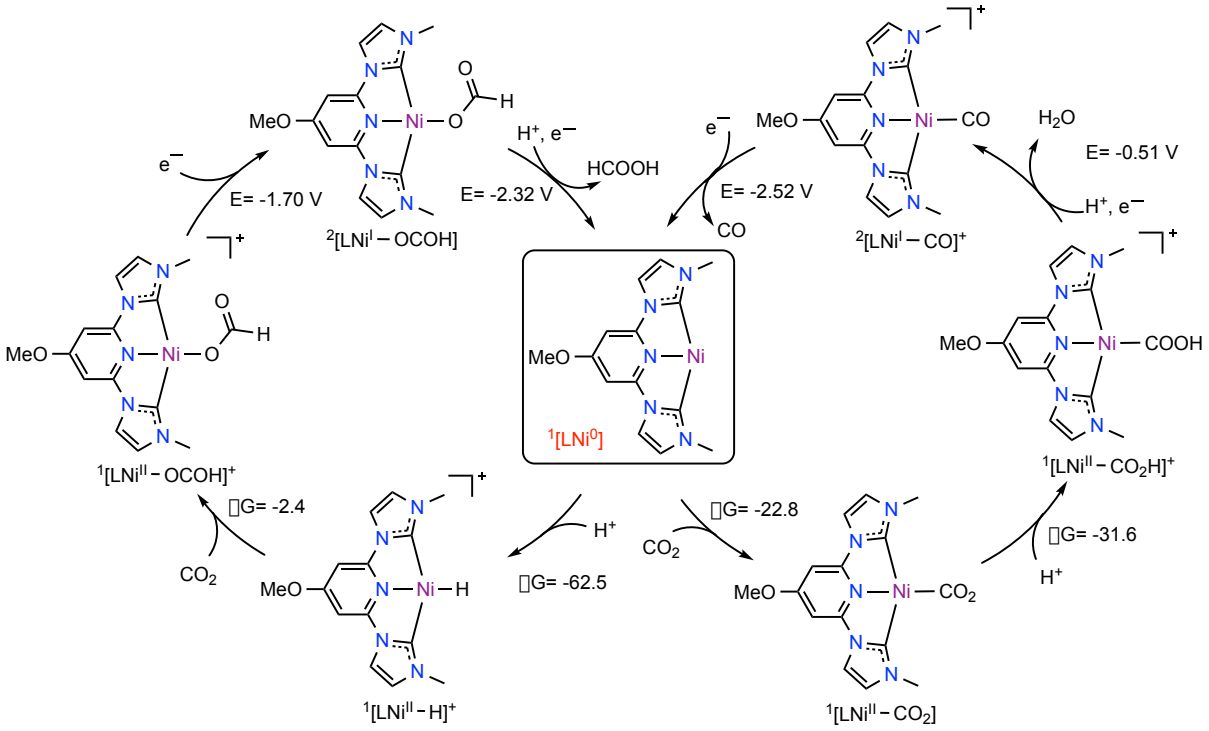

Scheme 3. Precatalyst **3^{OMe}** can undergo chloride loss and reduction under photocatalytic conditions to generate ^{1}[LNi^{0}] as a key intermediate with the catalytic pathways bifurcating at this point. Protonation of the metal center vs. CO_2 binding determines whether formic acid/formate vs. CO is formed. Given values without units are in kcal/mol.

In CO formation specifically, the energies of the individual steps in each of the six complexes are tabulated in **Tables S8 and S10**. During computational geometry optimization, the CO_2 molecule does not bind to ^{1}[LNi^{II}Cl]$^{+}$, ^{1}[LNi^{II}]$^{2+}$, or ^{2}[LNi^{I}]$^{+}$ complexes and their related geometries could not be located. It could be that all three complexes are cationic (or dicationic) and therefore lack sufficient nucleophilicity (but reduction could provide the necessary electron

density). If electron transfer events occur first to produce neutral $^2[LNi^ICl]$ or $^1[LNi^0]$ species, these species can bind CO_2. While it is challenging to reduce Ni^I to Ni^0 (the computed reduction potential $E(^2[LNi^I]^+/^1[LNi^0])$ is from -2.99 to -2.63 V vs. Fc^+/Fc), the chemical steps occurring from the $^1[LNi^0]$ complex are significantly more favorable than those with the $^2[LNi^ICl]$ complex. Both CO_2 coordination and proton transfer steps are exergonic with a $^1[LNi^0]$ cycle while they are slightly endergonic with the $^2[LNi^ICl]$ complex (**Tables S8 and S10**). It could be understood that nucleophilicity of $^1[LNi^0]$ is higher than the $^2[LNi^ICl]$ species due to its lower oxidation state.

After CO_2 binding to $^2[LNi^ICl]$ (**Scheme S1**), protonation produces a $^2[LNi^{III}Cl(COOH)]^+$ intermediate which is unusual oxidation state for nickel but it avoids the pathway involving halide loss. Then, a PCET step produces CO and water to regenerate the active species to complete a catalytic cycle. Compared with a concerted PCET mechanism, the stepwise electron transfer or proton transfer produces unstable intermediates whose geometries cannot be located. Because the complex is not coordinatively saturated, after the PCET step, CO can still bind to the metal center and form $^2[LNi^ICO]^+$ (**Table S10**). These steps (protonation and PCET) following CO_2 binding can occur via Ni^I/Ni^{III} cycles (without halide loss, Scheme S1) or Ni^0/Ni^{II} cycles (with halide loss, **Scheme 3**). It is important to note that the bound CO ligand decreases the energy demand for the reduction of Ni^I to Ni^0; the computed $E(^2[LNi^ICO]^+/^1[LNi^0CO])$ values range from -2.04 to -1.72 V vs Fc^+/Fc (**Table S10**, fifth column) and they are more negative without CO (**Table S10**, first column). Presumably, photodissociation of CO from either Ni^I or Ni^0 is plausible. Thus, reduction of $^2[LNi^ICO]^+$ to $^1[LNi^0CO]$ followed by photodissociation of CO provides an energetically feasible mechanistic pathway. Following CO loss from either $^2[LNi^ICO]^+$ or $^1[LNi^0CO]$, the catalytic cycle can continue (**Table S10**).

Self-Sensitized Nickel Catalysis

Without added photosensitizer $Ir(ppy)_3$, an excited state nickel complex is required to oxidize the sacrificial donor, BIH. The redox potential of $E_{BIH^+/BIH}$= -0.76 V vs Fc^+/Fc supports that BIH cannot be oxidized by any ground state nickel species. An excited nickel complex must play the role of photosensitizer in abstracting the electron from BIH and triggering the catalytically active species $^2[LNi^ICl]$ and possibly $^1[LNi^0]$. The computed reduction potential of the exited state complex, $E(^3[LNi^{II}Cl]^{*+}/^2[LNi^ICl])$ range from -0.79 to +0.05 V vs Fc^+/Fc (**Table S12**), shows a feasible process in oxidizing BIH (**Figure 9**). Therefore, the CO_2 reduction using the species $^2[LNi^ICl]$ leads to an active catalytic cycle. However, without considering the contribution of excitation of other complexes rather than starting from the halide-bound complex, the catalytic $^1[LNi^0]$ cycle is not able to occur. The electron transfer to reduce the excited state $^2[LNi^I]^{*+}$ species to $[LNi^0]$ is favorable but has less of a driving force vs. with $^3[LNi^{II}Cl]^{*+}$ as described above (computed reduction potentials for $E(^2[LNi^I]^{*+}/[LNi^0])$ range from -0.75 to -0.43 V vs Fc^+/Fc, **Table S10**). Because the TAS technique is limited to the precatalyst $[LNi^{II}Cl]^+$ species, it is challenging to relate the TAS data to the proposed mechanism involving excited states of intermediates generated from the precatalysts.

Accessing ^{3}MLCT states is consistent with the fact that other Ni(II) aryl halide complexes that undergo long-lived ^{3}MLCT excited states which engage in electron transfer reactions.[22] Bimolecular photoinduced electron transfer was proposed by Doyle and coworkers to describe how an excited-state nickel complex can transfer an electron to the ground state complex. However, in our case, an analogous mechanism generating the dication, $^2[LNi^{III}Cl]^{2+}$, requires a high amount of energy. Even considering the excitation energy, the computed reduction potentials $E(^2[LNi^{III}Cl]^{2+}/^3[LNi^{II}Cl]^+)$ range from 0.11 to 0.96 V vs Fc^+/Fc (see further details in **Table S12**).

Thus, we likely can rule out the possibility of forming a dication $^{2}[LNi^{III}Cl]^{2+}$ intermediate via a photoinduced electron transfer mechanism from monocation $^{1}[LNi^{II}Cl]^{+}$ species. Photoluminescence spectra were collected to characterize the electronic structure of the excited state. However, the data shows that the **3^{R}** and **4^{R}** complexes display no luminescence (**Figures S50-S52**). This result suggests that the excited singlet states undergo fast nonradiative decay to form non-luminescent triplet states as has been observed for other first row transition metal complexes.[51]

The Ni complexes are promising photocatalysts based on earth-abundant transition metals. To the best of our knowledge, the Ni-CNC pincer complexes studied here, may be the first nickel complexes that are active as self-sensitized photocatalysts for the CO_2 reduction reaction. Isotopic labeling studies confirm that external CO_2 is the source of CO generated from the photocatalysis CO_2 reduction reaction (**Figures S36-37**). Other first-row transition metal complexes have been reported which function as self-sensitized photocatalysts to drive the CO_2 reduction to CO.[10, 52-54] While some of these complexes are highly active (TON as high as 2,625)[54] we note that the presence of well-established photosensitizers as ligands to these metals (Fe and Cu) and the differences in conditions (including significant differences in light wavelength and intensity)[55] *versus* our work makes a direct comparison difficult. In addition, our complexes also showed significant formate production not only with the use of a PS (TON = 3,445) but also in the more challenging self-sensitized reaction (TON of 965).

Conclusions

Six new Ni(II) complexes of a CNC pincer ligand are reported, and these complexes are unusual for their excited state lifetimes in the microsecond range by TAS. In two complexes (**3^{OMe}** and **4^{OMe}**), a ligand π donor effect leads to exceptionally long-lived excited states that are not fully captured by our fitting parameters (τ, **Table 2**). The presence of such long lived excited states suggests that these may be suitable complexes for self-sensitized photocatalysis. Indeed, all six complexes are active catalysts for sensitized (with $Ir(ppy)_3$) photocatalytic CO_2 reduction and for self-sensitized CO_2 reduction, with **4^{Me}** being the most active catalyst.

This work points to a mechanism in which halide loss accelerates sensitized catalysis with $Ir(ppy)_3$ as the PS. Reduction of the PS by a sacrificial donor then results in electron transfer to Ni to produce neutral $^2[LNi^ICl]$ or $^1[LNi^0]$ species that can bind either H^+ first leading to formate or bind CO_2 first leading to CO. It appears that a mechanism invoking the $^1[LNi^0]$ species better aligns with formate being the major product. While halide loss is not required, it does result in a more exergonic catalytic cycle.

In contrast, self-sensitized CO_2 reduction only gives favorable electron transfer from BIH to the catalyst if occurring through the $^3[LNi^{II}\text{-}Cl]^{*+}$ excited state. Thus, some halide-bound species must be present in solution for favorable electron transfer from the sacrificial donor. Following electron transfer, CO_2 reduction can occur via cycles invoking Ni^I/Ni^{III} or Ni^0/Ni^{II}. Again, the mechanism involves a competition between protonation of the metal center vs. CO_2 coordination. The major product (formate) results from protonation leading to a hydride intermediate which inserts CO_2 and then reduction leads to release of formate or formic acid. Self-sensitized CO_2 reduction catalysis using visible light and first row metals is unusual and highly significant and can be explained through the stabilization of long-lived triplet excited states. These triplet excited

states are capable of oxidizing BIH which ultimately leads to the generation of formate as the major product and CO as the minor product, and both products have potential applications as solar fuels.

ASSOCIATED CONTENT

SI: Supporting Information

The Supporting Information is available free of charge at https://pubs.acs.org/doi/10.1021/acscatal.xxx

Experimental details on synthesis and characterization, single-crystal X-ray diffraction, cyclic voltammograms, transient absorption spectroscopy, photocatalysis, and computations (PDF)

Computational structures (XYZ)

Crystallographic information (CIF)

Acknowledgements

The authors thank the NSF (CHE-1800281, 1800214, 1800201, 2102416, 2102511, and 2102552; OIA-1757220) for funding this research. We thank NSF CHE MRI 1828078 and UA for the purchase of the SC XRD instrument. We thank NSF CHE MRI 1919906 and UA for the purchase of an NMR spectrometer. We thank Dr. Ken Belmore for assistance with the NMR experiments. We thank NSF MRI program (CHE 1726812, PI Cassady) and UA for the purchase of a MALDI TOF/TOF MS and Dr. Qiaoli Liang for MS experimental work. The computational work was completed with resources provided by the Mississippi State University High Performance Computing Collaboratory and the Mississippi Center for Super Computing Research.

Uncategorized References

1. Kang, P.; Chen, Z.; Brookhart, M.; Meyer, T. J., Electrocatalytic Reduction of Carbon Dioxide: Let the Molecules Do the Work. *Top. Catal.* **2015,** *58*, 30-45.
2. Su, X.; McCardle, K. M.; Panetier, J. A.; Jurss, J. W., Electrocatalytic CO2 reduction with nickel complexes supported by tunable bipyridyl-N-heterocyclic carbene donors: understanding redox-active macrocycles. *Chem. Commun.* **2018,** *54* (27), 3351-3354.
3. Hansen, J.; Sato, M.; Kharecha, P.; Beerling, D.; Berner, R.; Masson-Delmotte, V.; Pagani, M.; Raymo, M.; Royer, D. L.; Zachos, J. C., Target atmospheric CO2: where should humanity aim? *Open Atmos. Sci. J.* **2008,** *2* (Copyright (C) 2015 American Chemical Society (ACS). All Rights Reserved.), 217-231.
4. Hong, D.; Tsukakoshi, Y.; Kotani, H.; Ishizuka, T.; Kojima, T., Visible-Light-Driven Photocatalytic CO2 Reduction by a Ni(II) Complex Bearing a Bioinspired Tetradentate Ligand for Selective CO Production. *J. Am. Chem. Soc.* **2017,** *139* (19), 6538-6541.
5. Concepcion, J. J.; House, R. L.; Papanikolas, J. M.; Meyer, T. J., Chemical approaches to artificial photosynthesis. *Proc. Natl. Acad. Sci.* **2012,** *109* (39), 15560-15564.
6. Benson, E. E.; Kubiak, C. P.; Sathrum, A. J.; Smieja, J. M., Electrocatalytic and homogeneous approaches to conversion of CO_2 to liquid fuels. *Chem. Soc. Rev.* **2009,** *38* (1), 89-99.
7. Robert, M., Running the Clock: CO_2 Catalysis in the Age of Anthropocene. *ACS Energy Lett.* **2016,** *1* (1), 281-282.
8. Thoi, V. S.; Kornienko, N.; Margarit, C. G.; Yang, P.; Chang, C. J., Visible-Light Photoredox Catalysis: Selective Reduction of Carbon Dioxide to Carbon Monoxide by a Nickel N-Heterocyclic Carbene–Isoquinoline Complex. *J. Am. Chem. Soc.* **2013,** *135*, 14413-14424.
9. Takeda, H.; Koizumi, H.; Okamoto, K.; Ishitani, O., Photocatalytic CO_2 reduction using a Mn complex as a catalyst. *Chem. Commun.* **2014,** *50* (12), 1491-1493.
10. Rao, H.; Bonin, J.; Robert, M., Non-sensitized selective photochemical reduction of CO_2 to CO under visible light with an iron molecular catalyst. *Chem. Commun.* **2017,** *53* (19), 2830-2833.
11. Chan, S. L.-F.; Lam, T. L.; Yang, C.; Yan, S.-C.; Cheng, N. M., A robust and efficient cobalt molecular catalyst for CO_2 reduction. *Chem. Commun.* **2015,** *51* (37), 7799-7801.
12. Wang, J.-W.; Huang, H.-H.; Wang, P.; Yang, G.; Kupfer, S.; Huang, Y.; Li, Z.; Ke, Z.; Ouyang, G., Co-facial π–π Interaction Expedites Sensitizer-to-Catalyst Electron Transfer for High-Performance CO2 Photoreduction. *JACS Au* **2022**.
13. Beley, M.; Collin, J.-P.; Ruppert, R.; Sauvage, J.-P., Nickel(II)-cyclam: an extremely selective electrocatalyst for reduction of CO2 in water. *J. Chem. Soc., Chem. Commun.* **1984,** (19), 1315-1316.
14. Shirley, H.; Su, X.; Sanjanwala, H.; Talukdar, K.; Jurss, J. W.; Delcamp, J. H., Durable Solar-Powered Systems with Ni-Catalysts for Conversion of CO_2 or CO to CH_4. *J. Am. Chem. Soc.* **2019,** *141* (16), 6617-6622.
15. Burks, D. B.; Davis, S.; Lamb, R. W.; Liu, X.; Rodrigues, R. R.; Liyanage, N. P.; Sun, Y.; Webster, C. E.; Delcamp, J. H.; Papish, E. T., Nickel(II) pincer complexes demonstrate that the remote substituent controls catalytic carbon dioxide reduction. *Chem. Commun.* **2018,** *54*, 3819-3822.
16. Papish, E. T.; Das, S.; Silprakob, W.; Boudreaux, C. M.; Manafe, S., Proton Responsive and Hydrogen Bonding Ligands in Organometallic Chemistry. *Comprehensive Organometallic Chemistry IV* **2022,** *I*, 442-473.

17. Sheng, M.; Jiang, N.; Gustafson, S.; You, B.; Ess, D. H.; Sun, Y., A nickel complex with a biscarbene pincer-type ligand shows high electrocatalytic reduction of CO 2over H 2O. *Dalton Trans.* **2015,** *44* (37), 16247-16250.
18. Larsen, C. B.; Wenger, O. S., Photoredox Catalysis with Metal Complexes Made from Earth-Abundant Elements. *Chemistry – A European Journal* **2018,** *24* (9), 2039-2058.
19. Balzani, V.; Bergamini, G.; Campagna, S.; Puntoriero, F., Photochemistry and Photophysics of Coordination Compounds I. *Top Curr Chem* **2007**, 1-36.
20. Liu, Y.; Persson, P.; Sundström, V.; Wärnmark, K., Fe N-Heterocyclic Carbene Complexes as Promising Photosensitizers. *Accounts of Chemical Research* **2016,** *49* (8), 1477-1485.
21. Ting, S. I.; Garakyaraghi, S.; Taliaferro, C. M.; Shields, B. J.; Scholes, G. D.; Castellano, F. N.; Doyle, A. G., 3d-d Excited States of Ni(II) Complexes Relevant to Photoredox Catalysis: Spectroscopic Identification and Mechanistic Implications. *Journal of the American Chemical Society* **2020,** *142* (12), 5800-5810.
22. Shields, B. J.; Kudisch, B.; Scholes, G. D.; Doyle, A. G., Long-Lived Charge-Transfer States of Nickel(II) Aryl Halide Complexes Facilitate Bimolecular Photoinduced Electron Transfer. *J. Am. Chem. Soc.* **2018,** *140* (8), 3035-3039.
23. Thoi, V. S.; Chang, C. J., Nickel N-heterocyclic carbene–pyridine complexes that exhibit selectivity for electrocatalytic reduction of carbon dioxide over water. *Chem. Commun.* **2011,** *47* (23), 6578.
24. Wang, S.; Ren, F.; Qiu, Y.; Luo, M., Synthesis and catalytic activity of nickel(II) complexes of CNC pincer-type N-heterocyclic carbene ligands. *J. Organomet. Chem.* **2015,** *788*, 27-32.
25. Sun, Y.; Das, S.; Brown, S. R.; Blevins, E. R.; Qu, F.; Ward, N. A.; Gregory, S. A.; Boudreaux, C. M.; Kim, Y.; Papish, E. T., Ruthenium pincer complexes for light activated toxicity: Lipophilic groups enhance toxicity. *J. Inorg. Biochem.* **2022**, 112110.
26. Das, S.; Nugegoda, D.; Qu, F.; Boudreaux, C. M.; Burrow, P. E.; Figgins, M. T.; Lamb, R. W.; Webster, C. E.; Delcamp, J. H.; Papish, E. T., Structure Function Relationships in Ruthenium Carbon Dioxide Reduction Catalysts with CNC Pincers Containing Donor Groups. *Eur. J. Inorg. Chem.* **2020,** *2020* (28), 2709-2717.
27. Yang, L.; Powell, D. R.; Houser, R. P., Structural variation in copper(i) complexes with pyridylmethylamide ligands: structural analysis with a new four-coordinate geometry index, [small tau]4. *Dalton Trans.* **2007,** (9), 955-964.
28. Okuniewski, A.; Rosiak, D.; Chojnacki, J.; Becker, B., Coordination polymers and molecular structures among complexes of mercury(II) halides with selected 1-benzoylthioureas. *Polyhedron* **2015,** *90*, 47-57.
29. Das, S.; Nugegoda, D.; Yao, W.; Qu, F.; Figgins, M. T.; Lamb, R. W.; Webster, C. E.; Delcamp, J. H.; Papish, E. T., Sensitized and Self-Sensitized Photocatalytic Carbon Dioxide Reduction Under Visible Light with Ruthenium Catalysts Shows Enhancements with More Conjugated Pincer Ligands. *Eur. J. Inorg. Chem.* **2022,** *2022* (8), e202101016.
30. Yao, W.; Das, S.; DeLucia, N. A.; Qu, F.; Boudreaux, C. M.; Vannucci, A. K.; Papish, E. T., Determining the Catalyst Properties That Lead to High Activity and Selectivity for Catalytic Hydrodeoxygenation with Ruthenium Pincer Complexes. *Organometallics* **2020,** *39* (5), 662-669.
31. Das, S.; Rodrigues, R. R.; Lamb, R. W.; Qu, F.; Reinheimer, E.; Boudreaux, C. M.; Webster, C. E.; Delcamp, J. H.; Papish, E. T., Highly Active Ruthenium CNC Pincer

Photocatalysts for Visible-Light-Driven Carbon Dioxide Reduction. *Inorg. Chem.* **2019,** *58* (12), 8012-8020.
32. Satzger, H.; Zinth, W., Visualization of transient absorption dynamics – towards a qualitative view of complex reaction kinetics. *Chem. Phys.* **2003,** *295* (3), 287-295.
33. Henry, E. R.; Hofrichter, J., [8] Singular value decomposition: Application to analysis of experimental data. In *Methods Enzymol.*, Academic Press: 1992; Vol. 210, pp 129-192.
34. Hunt, L. A.; Das, S.; Lamb, R. W.; Nugegoda, D.; Curiac, C.; Figgins, M. T.; Lambert, E. C.; Qu, F.; Hammer, N. I.; Delcamp, J. H.; Webster, C. E.; Papish, E. T., Ruthenium (II) Complexes of CNC Pincers and Bipyridine in the Photocatalytic CO2 Reduction Reaction to CO Using Visible Light: Catalysis, Kinetics, and Computational Insights. *ACS Catalysis* **2023,** *13* (9), 5986-5999.
35. Rossini, E.; Bochevarov, A. D.; Knapp, E. W., Empirical Conversion of pKa Values between Different Solvents and Interpretation of the Parameters: Application to Water, Acetonitrile, Dimethyl Sulfoxide, and Methanol. *ACS Omega* **2018,** *3* (2), 1653-1662.
36. Dean, J. A., *Handbook of Organic Chemistry*. McGraw-Hill Book Co.: New York, NY, US, 1987; p 800.
37. Pegis, M. L.; Roberts, J. A. S.; Wasylenko, D. J.; Mader, E. A.; Appel, A. M.; Mayer, J. M., Standard Reduction Potentials for Oxygen and Carbon Dioxide Couples in Acetonitrile and N,N-Dimethylformamide. *Inorg. Chem.* **2015,** *54* (24), 11883-11888.
38. Costentin, C.; Drouet, S.; Robert, M.; Savéant, J.-M., A local proton source enhances CO_2 electroreduction to CO by a molecular Fe catalyst. *Science* **2012,** *338* (6103), 90-94.
39. Waldie, K. M.; Ostericher, A. L.; Reineke, M. H.; Sasayama, A. F.; Kubiak, C. P., Hydricity of Transition-Metal Hydrides: Thermodynamic Considerations for CO2 Reduction. *ACS Catal.* **2018,** *8* (2), 1313-1324.
40. Rodrigues, R. R.; Boudreaux, C. M.; Papish, E. T.; Delcamp, J. H., Photocatalytic Reduction of CO2 to CO and Formate: Do Reaction Conditions or Ruthenium Catalysts Control Product Selectivity? *ACS Appl. Energy Mater.* **2019,** *2*, 37-46.
41. Therrien, J. A.; Wolf, M. O.; Patrick, B. O., Electrocatalytic Reduction of CO 2with Palladium Bis-N-heterocyclic Carbene Pincer Complexes. *Inorg. Chem.* **2014,** *53* (24), 12962-12972.
42. DeLuca, E. E.; Xu, Z.; Lam, J.; Wolf, M. O., Improved Electrocatalytic CO2 Reduction with Palladium bis(NHC) Pincer Complexes Bearing Cationic Side Chains. *Organometallics* **2019,** *38* (6), 1330-1343.
43. Bonin, J.; Robert, M.; Routier, M., Selective and Efficient Photocatalytic CO 2Reduction to CO Using Visible Light and an Iron-Based Homogeneous Catalyst. *J. Am. Chem. Soc.* **2014,** *136* (48), 16768-16771.
44. Boudreaux, C. M.; Liyanage, N. P.; Shirley, H.; Siek, S.; Gerlach, D. L.; Qu, F.; Delcamp, J. H.; Papish, E. T., Ruthenium(II) complexes of pyridinol and N-heterocyclic carbene derived pincers as robust catalysts for selective carbon dioxide reduction. *Chem. Commun.* **2017,** *53*, 11217-11220.
45. Cope, J. D.; Liyanage, N. P.; Kelley, P. J.; Denny, J. A.; Valente, E. J.; Webster, C. E.; Delcamp, J. H.; Hollis, T. K., Electrocatalytic reduction of CO2 with CCC-NHC pincer nickel complexes. *Chem. Commun.* **2017,** *53* (68), 9442-9445.
46. Lee, S. K.; Kondo, M.; Okamura, M.; Enomoto, T.; Nakamura, G.; Masaoka, S., Function-Integrated Ru Catalyst for Photochemical CO_2 Reduction. *J. Am. Chem. Soc.* **2018,** *140* (49), 16899-16903.

47. Liyanage, N. P.; Dulaney, H. A.; Huckaba, A. J.; Jurss, J. W.; Delcamp, J. H., Electrocatalytic Reduction of CO2 to CO With Re-Pyridyl-NHCs: Proton Source Influence on Rates and Product Selectivities. *Inorg. Chem.* **2016,** *55* (12), 6085-6094.
48. De La Torre, P.; Derrick, J. S.; Snider, A.; Smith, P. T.; Loipersberger, M.; Head-Gordon, M.; Chang, C. J., Exchange Coupling Determines Metal-Dependent Efficiency for Iron- and Cobalt-Catalyzed Photochemical CO2 Reduction. *ACS Catal.* **2022,** *12* (14), 8484-8493.
49. Hagen, C. M.; Widegren, J. A.; Maitlis, P. M.; Finke, R. G., Is It Homogeneous or Heterogeneous Catalysis? Compelling Evidence for Both Types of Catalysts Derived from [Rh(η5-C5Me5)Cl2]2 as a Function of Temperature and Hydrogen Pressure. *J. Am. Chem. Soc.* **2005,** *127* (12), 4423-4432.
50. Hamlin, J. E.; Hirai, K.; Gibson, V. C.; Maitlis, P. M., Pentamethylcyclopentadienyl—rhodium and —iridium complexes: Part 35. Hydrogenation catalysts based on [(RhC5Me5)2(OH)3]+ and the border between homogeneous and heterogeneous systems. *J. Mol. Catal.* **1982,** *15* (3), 337-347.
51. Wegeberg, C.; Wenger, O. S., Luminescent First-Row Transition Metal Complexes. *JACS Au* **2021,** *1* (11), 1860-1876.
52. Rao, H.; Schmidt, L. C.; Bonin, J.; Robert, M., Visible-light-driven methane formation from CO2 with a molecular iron catalyst. *Nature* **2017,** *548* (7665), 74-77.
53. Yuan, H.; Cheng, B.; Lei, J.; Jiang, L.; Han, Z., Promoting photocatalytic CO2 reduction with a molecular copper purpurin chromophore. *Nat. Commun.* **2021,** *12* (1), 1835.
54. Yuan, H.; Du, J.; Ming, M.; Chen, Y.; Jiang, L.; Han, Z., Combination of Organic Dye and Iron for CO2 Reduction with Pentanuclear Fe2Na3 Purpurin Photocatalysts. *J. Am. Chem. Soc.* **2022,** *144* (10), 4305-4309.
55. Genoni, A.; Chirdon, D. N.; Boniolo, M.; Sartorel, A.; Bernhard, S.; Bonchio, M., Tuning Iridium Photocatalysts and Light Irradiation for Enhanced CO_2 Reduction. *ACS Catal.* **2017,** *7* (1), 154-160.